INTERNATIONAL JOURNAL FOR NUMERICAL METHODS IN FLUIDS
Int. J. Numer. Meth. Fluids 2002; **38**:609–624 (DOI: 10.1002/fld.200)

Application of local grid refinement to vortex motion due to a solitary wave passing over a submerged body

Chii-Jau Tang[1,*,†] and Jyh-Hwa Chang[2,‡]

[1]*Department of Hydraulics and Ocean Engineering, National Cheng Kung University, Tainan, Taiwan, Republic of China*
[2]*Water Resources Research Center, Taichung, 40100, Taiwan, Republic of China*

SUMMARY

A numerical method based on the streamfunction–vorticity formulation is applied to simulate the two-dimensional, transient, viscous flow with a free surface. This method successfully uses the locally refined grid in an inviscid–viscous model to explore the processes of vortex formation due to a solitary wave passing over a submerged bluff body. The two particular bodies considered here are a blunt rectangular block and a semicircular cylinder. Flow visualization to track dyelines is carried out in the laboratory in order to confirm the validity of the numerical results. Numerical results examined by different grid configurations ensure the locally refined grid to be useful in practical application. Flow phenomena, including the vortex motion and wave patterns during non-linear wave–structure interaction, are also discussed. Copyright © 2002 John Wiley & Sons, Ltd.

KEY WORDS: boundary fitted grid; local grid refinement; solitary wave; vortex motion

1. INTRODUCTION

The characteristics of a non-linear, long wave interacting with a hydraulic structure are important to many coastal problems. An incident solitary wave upon a submerged structure in the shallow water region has been studied [1–4] using the weakly non-linear, long wave equations in recent years. To avoid the tedious higher-order correction to these simplified equations, some researchers [5–8] have chosen to study the full non-linear equations instead. Nevertheless, these investigations apparently contribute less in studying flows with viscous effects, in association with blunt body shape, shallow submergence of the structure interacted with a large-amplitude wave in shallow water. To analyze viscous effects on wave–structure interaction, a numerical method based on the streamfunction–vorticity

---

[*] Correspondence to: C.J. Tang, California Institute of Technology, 104-44 Engineering Science, Pasadena, CA 91125, U.S.A.
[†] E-mail: cjtang@mail.ncku.edu.tw
[‡] E-mail: changbox@pchome.com.tw

Contract/grant sponsor: National Science Council of ROC; contract/grant number: N5C88-2611-E006-023

Received 21 December 1999
Revised 9 October 2000

(ψ–ω) formulation was developed to ally with a boundary fitted grid system. Using this accurate method with a globally fine grid, the authors [9] succeeded in exploring not only the free-surface evolution but also the entire flow pattern. These include the flow separation from a solid surface, vortex-free surface interaction, wave radiation, etc.; all induced by a large solitary wave passing over a high bluff body. Although the application of streamfunctions to a three-dimensional flow is still possible [10], the ψ–ω formulation is more convenient and believably optimal for the two-dimensional viscous flow coupled with complicated conditions on the irregular boundaries, as compared with other viscous models. However, the formulation is not yet the most economic in computations because a unified viscous model with a globally fine grid is applied in the whole region, as was used by the referred article [9].

Within the entire computational domain, solution accuracy may request a fine grid only in a small region where steep gradients in physical variables appear. For example, the boundary layer near a solid surface and the free surface region for wave problems are just a couple of such regions. The former is obvious without further explanations and the latter has its own reasons based on physics. As a rule of thumb, a regular periodic wave profile usually needs at least ten nodes within a wavelength to resolve its shape and describe its transience on the free surface. On the other hand, a coarser grid applied in most flow regions is preferable from a computer economics standpoint. To avoid compromising solution accuracy for computer economics or vice versa, one may use the local grid refinement technique in the analysis instead of using a globally fine grid in the whole domain. This technique has been proved to be efficient in calculating many flow problems [11–18]. As to the water wave problems, the authors also verified the local grid refinement technique to be useful in simulating the solitary wave train generated by a submerged body accelerated in an inviscid fluid [19].

In the present study, the finer grids are locally embedded along the free surface and in the vicinity of the bluff body, and a coarser base grid is widely distributed in the most other region. Moreover, a viscous–inviscid hybrid model is also considered. In order to grasp the most physical significance and reduce CPU time, both the viscous flow solution and the inviscid flow solution are calculated independently in various regions by using different numerical methods with their own meshes, as will be described later. Then both solutions are matched to construct a complete one such that all variables at the region interfaces are continuous. With these techniques, the present hybrid model can efficiently resolve the complete physical phenomena, with the same accuracy as in the previous work [9], which solved the entire viscous solution in a globally fine grid system. To exhibit the feasibility of the proposed numerical method, this paper investigates two different submerged bluff structures, namely a rectangular block and a semicircular cylinder. The former structure is also studied in the laboratory by the physical model test. Flow visualized by colored dyelines (streaklines) around the block is photographed to verify the numerical result. In the numerical simulation the trajectory of massless Lagrangian particles is tracked down in the flow field by the inverse mapping method in the computational domain. In all, several objectives are worth emphasizing in the proposed numerical method: (i) to develop the technique of local grid refinement together with the inviscid–viscous flow model; (ii) to perform grid refinement in an evolving boundary conformed grid system for unsteady free-surface flow problems; (iii) to use a hybrid grid system in combination with the stationary and the moving grids for strong wave–structure interaction problems; and (iv) to demonstrate the visualized flow pattern by using the inverse particle tracing technique.

2. MATHEMATICAL FORMULATIONS

Consider the vortex motion induced by an incident solitary wave passing over a bluff body submerged in water. The flow is assumed to be two-dimensional, viscous and incompressible. The fluid velocity vector $\underline{u} = (u, v)$ is represented by the Cartesian (x, y) components, respectively. Although the flow field is governed by the equation of continuity and the Navier–Stokes equations, it is easier to analyze the streamfunction (ψ)–vorticity (ω) field for a two-dimensional flow. The relationships among velocity, streamfunction, and vorticity are $(u, v) = (\psi_y, -\psi_x)$ and $\omega = v_x - v_y$, where subscripts imply partial differentiation. In order to describe the transient free-surface geometry and to evaluate boundary conditions accurately, it is useful to apply the general curvilinear co-ordinates $(\xi(x, y, t), \eta(x, y, t); \tau = t)$ to construct a boundary conformed grid system. Since the curvilinear co-ordinates are well structured in data storage and easy to deal with derivatives in formulation, the computer programming for models with a boundary fitted system is much simpler than that using the unstructured grids. Several examples of adopting the curvilinear co-ordinates for the time-dependent free surface flow are referred [20, 21]. By choosing fluid density ρ, undisturbed water depth H, and gravitational acceleration g as referred variables in dimensional analysis, the non-dimensional governing equations in the curvilinear grid system are

$$\nabla^2\omega = Re(\omega_\tau + U\omega_\xi + V\omega_\eta) \tag{1}$$

$$\nabla^2\psi = -\omega \tag{2}$$

where the dimensionless parameter $Re = (\rho H\sqrt{gH})/\mu$ is the Reynolds number with dynamic viscosity, μ, of the fluid. In the above equations, the Laplacian operator ∇^2 and the contravariant velocity (U, V) in the (ξ, η) system are defined by

$$\nabla^2 = g^{11}\frac{\partial^2}{\partial\xi^2} + 2g^{12}\frac{\partial^2}{\partial\xi\partial\eta} + g^{22}\frac{\partial^2}{\partial\eta^2} + f^1\frac{\partial}{\partial\xi} + f^2\frac{\partial}{\partial\eta} \tag{3}$$

$$(U, V) = \frac{(\psi_\eta - x_\tau y_\eta + y_\tau x_\eta, -\psi_\xi + x_\tau y_\xi - y_\tau x_\xi)}{J} \tag{4}$$

Here $g^{11} = (x_\eta^2 + y_\eta^2)/J^2$, $g^{22} = (x_\xi^2 + y_\xi^2)/J^2$, $g^{12} = -(x_\xi x_\eta + y_\xi y_\eta)/J^2$, $f^1 = \{(Jg^{11})_\xi + (Jg^{12})_\eta\}/J$, and $f^2 = \{(Jg^{12})_\xi + (Jg^{22})_\eta\}/J$ are geometric coefficients, and $J = x_\xi y_\eta - y_\xi x_\eta$ is the Jacobian of transformation. Since the grid is time-dependent, U and V in Equation (4) have additional terms associated with grid speed (x_τ, y_τ) to justify inertial convection of vorticity transport in Equation (1). Similar justification is also done on the convection of the free-surface conditions, as described below.

That an incident solitary wave passes over a submerged bluff body is an initial boundary valued problem in this analysis. The associated conditions are summarized as follows:

Boundary conditions on the free surface: On $y = \zeta(x, t)$

$$\omega = 0 \tag{5a}$$

Kinematic condition (*KC*):

$$\psi_\xi + \zeta_\tau x_\xi = x_\tau \zeta_\xi \tag{5b}$$

Dynamic condition (*DC*):

$$\psi_{\xi\tau}(Jg^{12}) + \psi_{\eta\tau}(Jg^{22}) + \psi_{\xi}\tilde{A} + \psi_{\eta}\tilde{B} + (u - x_{\tau})u_{\xi} + (v - \zeta_{\tau})v_{\xi} + \zeta_{\xi} = 0 \tag{5c}$$

with

$$\tilde{A} = -(x_{\eta}/J)_{\tau}x_{\xi} - (y_{\eta}/J)_{\tau}y_{\xi}, \quad \tilde{B} = (x_{\xi}/J)_{\tau}x_{\xi} + (y_{\xi}/J)_{\tau}y_{\xi}$$

Solid-surface conditions:

$$\psi = \psi_0(=0) \tag{6a}$$

$$\psi_{\eta} = 0 \tag{6b}$$

$$\omega = -g^{22}\psi_{\eta\eta} \tag{6c}$$

Far upstream and downstream boundary conditions:

$$\psi_{\xi} = 0 \tag{7a}$$

$$y_{\xi} = 0 \tag{7b}$$

$$\omega_{\xi} = 0 \tag{7c}$$

Initial conditions: An initial solitary wave is imposed so far away from the bluff body that the initial condition of ψ^0 can be obtained by ignoring the fluid viscosity. We apply an incident solitary wave profile of amplitude A_0 and celerity C, moving in the positive x-direction with initial peak centered at $x = x_0$, based on Grimshaw's third-order formula [22]

$$\zeta^0 = A_0 \operatorname{sech}^2 X[1 - \tfrac{3}{4}A_0 \tanh^2 X + A_0^2 \tanh^2 X(\tfrac{5}{8} - \tfrac{101}{80} \operatorname{sech}^2 X \tanh^2 X)] \tag{8}$$

in which

$$X = \sqrt{\tfrac{3}{4}A_0}(1 - \tfrac{5}{8}A_0 + \tfrac{71}{128}A_0)(x - x_0)$$

Therefore, the streamfunction on the free surface (say, ψ_f^0) at $t = 0$ is given by

$$\psi_f^0 = C\zeta^0 = (1 + \tfrac{1}{2}A_0 - \tfrac{3}{20}A_0^2 + \tfrac{3}{56}A_0^3)\zeta^0 \tag{9}$$

The initial condition of ψ^0 is then obtained from the numerical solution of the potential flow with all associated boundary conditions (9), (6a) and (7a) in a boundary fitted grid system, which will be discussed later.

3. NUMERICAL METHOD

3.1. *Discretization and solution procedure by unified grid* (*without refinement*)

In the present study, the vorticity transport equation (1) is discretized by the finite analytic (FA) method, which is to incorporate the analytic solution of the linearized convection–diffusion transport equation into a discretization expression for calculation. To do that, first use the nodal values of (U, V), ψ_{ξ}, ψ_{η} and all geometric coefficients to linearize Equation (1), and replace the time derivative ω_t with the first-order backward difference. In order to find the unique solution for this linearized equation in a small cell, one also needs to approximate the cell boundary conditions by exponential-linear functions, which are obtained by interpolating values of neighboring nodes around the cell. By using superscript indices n and $n+1$ to represent the time levels $(n)\Delta\tau$ and $(n+1)\Delta\tau$, respectively, and subscripts E, W, N, S, and C for the nodes surrounding p, the analytical solution of ω_p^{n+1} at the $(n+1)$ time level can be written as

$$\begin{aligned}\omega_p^{n+1} = {} & (C_{\mathrm{EC}}\omega_{\mathrm{EC}}^{n+1} + C_{\mathrm{WC}}\omega_{\mathrm{WC}}^{n+1} + C_{\mathrm{NC}}\omega_{\mathrm{NC}}^{n+1} + C_{\mathrm{SC}}\omega_{\mathrm{SC}}^{n+1} + C_{\mathrm{NE}}\omega_{\mathrm{NE}}^{n+1} + C_{\mathrm{NW}}\omega_{\mathrm{NW}}^{n+1} \\ & + C_{\mathrm{SE}}\omega_{\mathrm{SE}}^{n+1} + C_{\mathrm{SW}}\omega_{\mathrm{SW}}^{n+1} + C_p S_p) \bigg/ \left(1 + C_p \frac{Re}{\Delta\tau}\right)\end{aligned} \tag{10}$$

where these FA coefficients are [23]

$$\begin{aligned}
C_{\mathrm{EC}} &= \mathrm{e}^{-\alpha}E_{\mathrm{b}}, \quad C_{\mathrm{WC}} = \mathrm{e}^{\alpha}E_{\mathrm{b}}, \quad C_{\mathrm{NC}} = \mathrm{e}^{-\beta}E_{\mathrm{a}}, \quad C_{\mathrm{SC}} = \mathrm{e}^{\beta}E_{\mathrm{a}}, \quad C_{\mathrm{NE}} = \mathrm{e}^{-\alpha-\beta}E_{\mathrm{c}} \\
C_{\mathrm{NW}} &= \mathrm{e}^{\alpha-\beta}E_{\mathrm{c}}, \quad C_{\mathrm{SE}} = \mathrm{e}^{-\alpha+\beta}E_{\mathrm{c}}, \quad C_{\mathrm{SW}} = \mathrm{e}^{\alpha+\beta}E_{\mathrm{c}} \\
C_p &= \frac{\tanh\alpha}{2\alpha g_p^{11}}(1 - 2\cosh\beta E_{\mathrm{a}}), \quad S_p = \omega_p^n \frac{Re}{\Delta\tau} + \frac{1}{2} g_p^{12}(\omega_{\mathrm{NE}}^{n+1} + \omega_{\mathrm{SW}}^{n+1} - \omega_{\mathrm{SE}}^{n+1} - \omega_{\mathrm{NW}}^{n+1}) \\
E_{\mathrm{a}} &= \sum_{m=1}^{\infty} \frac{(-1)^{m+1} 2\lambda_m \alpha \cosh\alpha \coth\alpha}{[\alpha^2 + \lambda_m^2]^2 \cosh\sqrt{(\alpha^2 + \lambda_m^2)/\kappa + \beta^2}}, \quad \lambda_m = (m - 0.5)\pi, \quad m = 1, 2, \ldots, \infty \\
E_{\mathrm{b}} &= \left[1 + \frac{\beta\coth\beta}{\alpha\kappa\coth\alpha}(2\cosh\beta E_{\mathrm{a}} - 1)\right] \bigg/ (2\cosh\alpha) \\
E_{\mathrm{c}} &= (1 - 2\cosh\beta E_{\mathrm{a}} - 2\cosh\alpha E_{\mathrm{a}})/(4\cosh\alpha\cosh\beta) \\
\kappa &= g_p^{11}/g_p^{22}, \quad \alpha = -(f_p^1 - Re\,U_p)/2\sqrt{g_p^{11}}, \quad \beta = -(f_p^2 - Re\,V_p)/2\sqrt{g_p^{22}}
\end{aligned}$$

The application of the FA method overcomes numerical difficulties, such as numerical oscillations, non-physical damping, etc., caused by inertial convection in Equation (1), for it conveys most of the physical significance involved in the original partial differential equations. This will be superior to most limiter-based schemes in numerical practice. The conceptual discussion of the one-dimensional FA (exponential) scheme for a convection–diffusion equation is referred to Patankar's book [24]. The FA method has been successfully applied to many internal and external viscous flow problems without a free surface [25, 26]. In addition to using the FA method for calculating the ω field in the present study, the second-order five-point central differences are applied to the Poisson equation (2) for solving the ψ field inside the flow region. Because the grid resolution applied for solving ψ is controlled cautiously so as to preserve the specified accuracy of our solution, this primitive solver will not introduce a source of inaccuracy in the present study.

On the boundaries, one suffers two numerical difficulties in calculation, namely, the treatment of the free-surface conditions and the determination of the wall vorticity. It is worthwhile to describe them in detail. For the free-surface boundary conditions, time- and

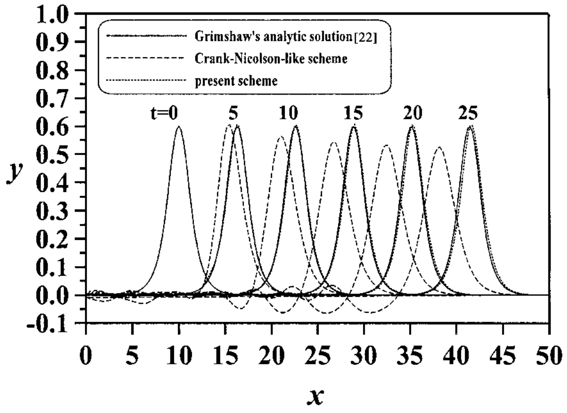

Figure 1. Comparison of the free-surface profiles obtained by the present two-step scheme (dotted lines); Crank–Nicholson scheme (dashed lines); and the analytic solution of Grimshaw [22] (solid lines).

η-derivatives discretized with first-order differences, and ξ-derivatives with the central difference of second-order accuracy. Hence, the free-surface DC, Equation (5c), is expressed by the two-stage form

$$\frac{\psi_\xi^{n+1}-\psi_\xi^n}{\Delta\tau}(Jg^{12})^* + \frac{\psi_\eta^{n+1}-\psi_\eta^n}{\Delta\tau}(Jg^{22})^* + \psi_\xi^*\tilde{A}^* + \psi_\eta^*\tilde{B}^* + \left(u^* - \frac{x^{n+1}-x^n}{\Delta\tau}\right)u_\xi^*$$
$$+ \left(v^* - \frac{\zeta^{n+1}-\zeta^n}{\Delta\tau}\right)v_\xi^* + \zeta_\xi^* = 0 \tag{11}$$

By setting $^* = n$ and $n+1$ in Equation (11) and solving them for ψ^{n+1}, one obtains the first-stage value $\psi_{(1)}$ and the second-stage value $\psi_{(2)}$, respectively. Finally, one gets the free-surface streamfunction ψ_f by taking the arithmetic average of $\psi_{(1)}$ and $\psi_{(2)}$. In a similar manner, one can also compute the free-surface elevation ζ from the free-surface KC (5b) by using the two-stage starred form

$$\frac{\zeta_i^{n+1}-\zeta_i^n}{\Delta\tau}x_\xi^* + \psi_\xi^* = 0 \tag{12}$$

Actually, the present two-stage treatment of the KC form is identical to the well-known Crank–Nicholson (CN) scheme in light of the linear essence in the KC. However, for the non-linear DC, the present scheme rather differs from the CN scheme. To see the difference, one compares in Figure 1 the evolved surface profiles obtained by both schemes for a solitary wave (of initial amplitude $A_0 = 0.6$) traveling along a uniform channel without friction. It is easily seen from this figure that the numerical result obtained by the present scheme is much better than that by the CN scheme.

The above *inviscid free-surface flow coupling* consists of ψ inside the flow region interacting with ψ_f and ζ on the free surface, and consequently, involves an evolving grid system in

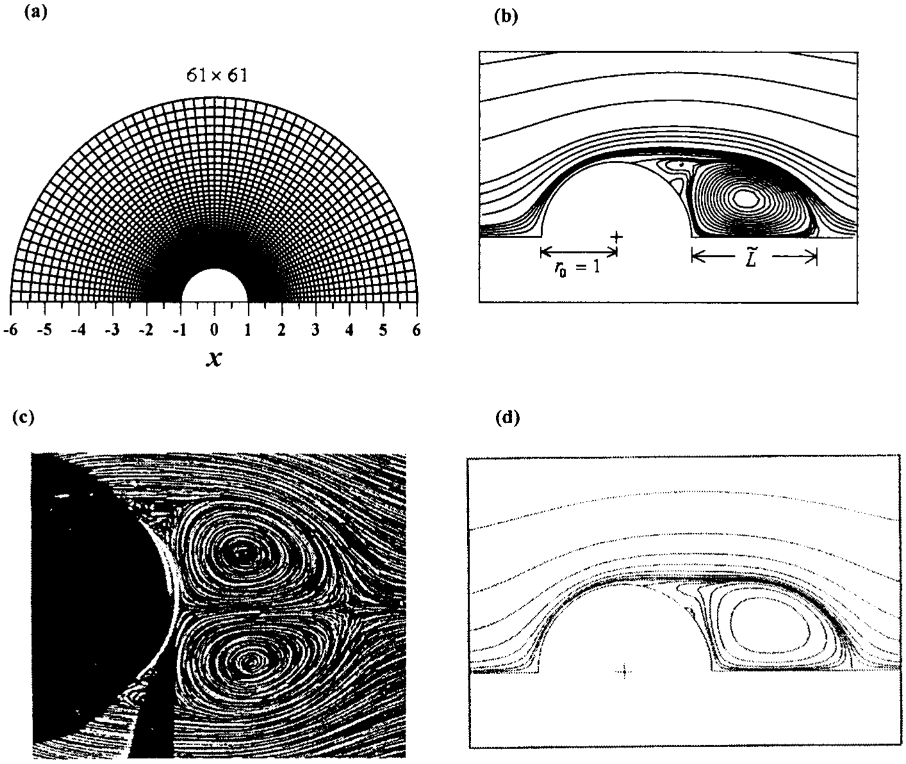

Figure 2. Streamline patterns for a uniform flow past a circular cylinder: (a) applied grid system; (b) present numerical solution; (c) experiment of Bouard and Coutanceau [27]; and (d) numerical solution of Chang and Chern [28].

light of the existence of a moving free surface. On the other hand, the viscous flow coupling contains the interior ψ–ω field interacting with the wall vorticity in response to fluid viscosity. After invoking the second-order central difference scheme and the no-slip and impermeable conditions, $\psi = \psi_0 = 0$ and $\psi_\eta = (\psi_1 - \psi_{-1})/2 = 0$, respectively, on a solid wall, Equation (6c) reduces to

$$\omega_0 = -g^{22}(\psi_1 + \psi_{-1} - 2\psi_0) = -2g^{22}\psi_1 \tag{13}$$

which is of second-order accuracy. Here, subscripts ‘0’, ‘1’ and ‘-1’ denote nodes on the wall and on its two opposite sides respectively. Because the coupling of ψ and ω appear in Equations (1) and (2) and the wall vorticity in condition (13), the iterative process is necessary to get the convergent solution of them. In order to examine the validity of the present ψ–ω model, we calculate a uniform flow passing a circular cylinder at the diameter-based Reynolds number $Re_\mathrm{D} = 550$ ($= 2Re$). At this Reynolds number, a laminar boundary layer quickly thickens along the curved wall and finally separates from wall surface to form a symmetric vortex bubble behind the body. Due to the symmetry, a half of fluid domain is enough for the numerical study. Figure 2(a) shows the applied mesh and Figure 2(b) exhibits the calculated

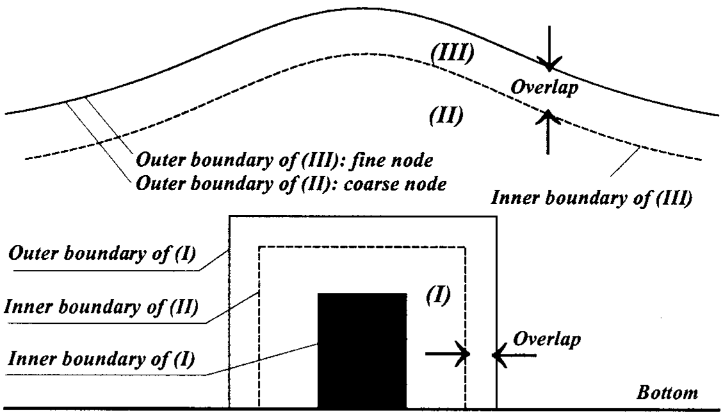

Figure 3. Key sketch of the decomposed regions and their boundaries.

streamlines. The recirculating flow is excellently consistent with the experiment by Bouard and Coutanceau [27] (in Figure 2(c)) and the numerical result by Chang and Chern [28] (in Figure 2(d)). The application of this model to the viscous flow with a free surface was also studied in a unified grid system by the authors [9].

The upstream and downstream boundary conditions are simply treated by the first-order one-sided FD schemes. From numerical experiments [9], this treatment does not found to introduce the false numerical reflection if both boundaries are far enough away from the body.

To summarize the solution procedure in the unified grid system, one first calculates ψ_f from the two-stage DC, Equation (12) and ω_0 from Equation (13) to obtain the converged ψ–ω field inside the flow region by using the FD and FA methods through iteration. One then updates the free-surface elevation ζ from the two-stage KC, Equation (12), and regenerates the grid system to conform the free surface and other boundaries. In this new grid system, one calculates again the ψ–ω fields on the boundary and within the flow region, as described above. After iterating the solution of ψ, ω and ζ until the grid system and the flow field are all converged, one proceeds with the calculation to the next time step.

3.2. Mesh generation and solution procedure with grid refinement

Overall grid structure consists of a hybrid of three grid systems in which the coarse base system globally covers the background domain and the two locally refined ones wrap around the bluff body and the free surface, as shown in Figure 3. We first construct the base grid systems to conform the free surface, body faces, and upstream and downstream boundaries. All η-lines are uniformly distributed and are kept vertical and fixed all the time for simplicity, while some ξ-lines can be deformed with time. Then select some base grid lines to enclose the interested regions near the body and near the free surface for further refinement. Hence, all of three grid systems are fitted with their regional boundaries. These boundary fitted grids are constructed by using either algebraic generation (AG) or elliptic generation (EG) methods, depending on the boundary configuration. The AG grid is obtained by interpolating nodes, linearly or exponentially distributed along grid-lines, between the upper and lower bounds

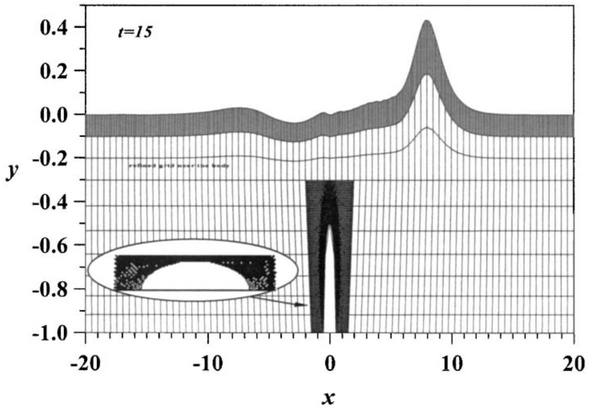

Figure 4. Typical grid configuration for calculating a solitary wave passing over a circular cylinder with local grid refinement at time $t = 15$.

of the region. On the other hand, the EG grid is obtained from the iterative solution of the Laplace equations $\nabla^2 x = 0$ and $\nabla^2 y = 0$ with the Dirichlet boundary conditions, similar to the solution procedure for ψ. In practice, the AG grid generation is more economic in computing than the EG grid. The employment of the EG grid is only for the refined region around the semi-circular cylinder, as shown typically in Figure 4. Remind that the present grid systems are evolved with the free surface and consequently, the relative grid motion will affect vorticity, streamfunction, and the free-surface quantities node by node through Equations (1), (2), (5b) and (5c). The fully iterative procedure is therefore necessary at every time step to get a convergent solution of the flow field and grid systems, which means that the solution is time-accurate for both the free-surface elevation and the related flow field. The numerical treatment for these three grid regions (refer to Figure 3) are discussed as follows:

Region I (*Refined grid system near the bluff body for viscous flow coupling*): Refinement is carried out by adding nodal points on the regional boundaries and then by generating grids inside the region by using the AG or the EG method. This grid system is always stationary to save computing time. The FA method for ω with the FD scheme for ψ is carried out for solving the complete ψ–ω equations by a finer mesh.

Region II (*Base grid system*): The initial base grid is uniformly distributed by the AG method within the global numerical domain. Later it is allowed only the upper part of ξ-grids to move with the free surface, but keeps the lower part fixed all the time. The five-point central FD method is used to solve the Laplace equation for ψ by the base (coarse) mesh under the inviscid assumption.

Region III (*Refined grid system near the free surface for free-surface flow coupling*): This region contains a layer enclosed by two uppermost base-grid lines (ξ-lines) at the free surface. The grid system is refined only in one way along the free surface. The grid in this region moves with the free surface. Under the inviscid flow consideration, the two-stage FD scheme for both ψ and ζ is employed to solve the fully non-linear free-surface conditions by the finer grid.

In addition, it is required to patch the two joint solutions across the overlap interface (with thickness of one coarse grid size) so that the continuity of flow and grid variables is satisfied there. As referred to in Figure 3, there are two procedures used to perform the patch across the interface. The coarser-to-finer grid procedure is generally called interpolation while the finer-to-coarser grid procedure is called restriction. For example, at the overlap interface between Regions II and III (interface II–III in brief), one can *interpolate* the inner boundary values of ψ_{f-1} and y_{f-1} for Region III from the base-grid solution by third-degree polynomials. After solving the free-surface conditions with these interpolated values, the solution in Region III is *restricted* to the free-surface values of ψ_f and ζ, by simply taking the nodal values at a coarse grid. These are the outer boundary conditions necessary for seeking the solution of ψ in Region II and for regenerating the new grid systems. The patch by both interpolation and restriction can be proceeded further through iteration until the solution in all regions is converged.

A similar patching technique can be applied to the interface I–II except now the grid in Region I is fixed with time. The employment of a thoroughly fixed finer mesh system in Region I improves both accuracy and efficiency in resolving the salient features of vortex flow behind the body. Again, a bilinear interpolation method is performed by patching the interfacial solution from the base-grid region, Region II, to the locally refined grid region, Regions I. Note that the only patched quantity needed is ψ (i.e., ψ_b and ψ_{b+1}) since we apply $\omega = 0$ and a fixed grid at the interface I–II. It will be seen later in this paper that this application indeed saves a lot of computing time without the penalty for accuracy of the flow solution.

The solution procedure in the locally refined grid system slightly differs from that in the unified grid. First, one has to interpolate the interfacial values of ψ_{f-1}, y_{f-1}, and ψ_{b+1} as the boundary values for the refined grid Regions III and I. Using the FD or the FA method with the finer grids, one gets ψ_f from the DC in Region III, and the ψ–ω field in flow Region I. After restricting ψ_f and ψ_b, one can solve the inviscid solution of ψ in Region II through iteration of the patch procedures for both the free-surface coupling in Region III and the viscous flow coupling in Region I. The converged values of ψ_f are used to update and, in consequence, to regenerate the two grid systems in Regions II and III. Again, one still necessarily repeats the whole solution procedures described above. Several iterations are necessary to get enough accuracy in the flow solution and grid systems at every time step.

3.3. Particle tracing technique

In order to compare with the experimental visual result, it is necessary to introduce particle tracers in the numerical result to imitate the flow motion. During tracing the trajectory of particles, we need to integrate the displacement of particles with respect to time through interpolation of their instantaneous velocities. In computational fluid dynamics, the algorithm of the particle tracing method (PTM) [29] is often carried out for a fixed-grid system in the physical space by the area-weighting scheme. Instead, for a moving boundary problem, the inverse PTM is so developed that the PTM is performed in the numerical domain and the trajectory of particles is then mapped inversely to the related physical space. This IPTM algorithm has the following advantages for the present grid system: (1) the procedure to find the marker location in the fixed numerical domain is simple and efficient, without invoking a searching procedure necessary; (2) it is convenient to estimate the other physical quantities of interest at the particle position by the common weighting factors in a cell; and

(3) the accuracy of the tracer movement is automatically justified along with the applied grid configuration as needed.

4. RESULT AND DISCUSSION

In the present study, two typical bluff bodies are considered, namely, a rectangular block with length $2H$ by height $0.5H$, and a semicircular cylinder with radius of $0.5H$ (here H is the undisturbed water depth). Flow simulations by either numerical or experiment work are all performed at the Reynolds number $Re = 82\,000$. In numerical calculation, a time step of $\Delta\tau = 0.1$ is employed. Streaklines, streamlines, and equivorticity lines are tracked to investigate the vortex motion. First, a solitary wave starts from $x_0 = -15$ to incident upon the rectangular block, as described the first bluff body above. The total computational domain is confined within $-30 \leqslant x \leqslant 30$. To illustrate the sensitivity of mesh resolution on the transient behavior of the numerical solution, the free-surface profiles and streamline contours are presented at $t = 17$ in Figure 5. Those results are obtained from three various grid configurations. The first two are of unified grids in the viscous flow model, while the other uses locally refined grids in the hybrid inviscid–viscous flow model. As noted in the legend, Δx, Δy represent the approximated spatial grid sizes for the background grid, Δx_b, Δy_b for the bluff grid (Region I), and Δx_f for the free-surface grid (Region III). Grid nodes are also plotted as dots for convenience of comparison. The first result shown in Figure 5(a) is calculated by 121×11 (coarse unified) grid, and the second result for 601×41 (fine unified) grid is shown in Figure 5(b). In Figure 5(c), there is a coarse background mesh of 121×11 grid with two locally refined systems of 61×29 grid around the bluff body and 601×2 grid near the free surface. Here the unified grid result in Figure 5(b) is taken as the referred solution for comparison, because this result has the best resolution among the three and it does not have any detectable change for further grid refinement. The improvement of the locally refined grid result in Figure 5(c) is significant, especially as one compares the vortex bubble and the free-surface profile with Figures 5(a) and 5(b). The capability of using this locally refined grid to resolve the physical detail is therefore demonstrated. Furthermore, the location of the grid interface I–II is chosen to be away from the body so that the viscous effect is not important to the solution in Region II. Hence, the inviscid–viscous hybrid scheme applied here would avoid serious penalty for accuracy of the numerical result.

The unsteady vortex pattern behind the block is visualized much easier by the dyeline than by the streamline. The evolution of tracked dyelines from the experiment and the corresponding numerical results are demonstrated in Figure 6. The upper picture from the experimental observation [9] was taken in a water flume 12 m in length, 40 cm in depth and 40 cm in width. The flow condition was set up to the water depth $H^* = 8$ cm, and an initial solitary wave of $A_0 = 3.2$ cm (i.e., $A_0 = 0.4$) with a rectangular cylinder, of sectional dimension 16 cm in length and 3.98 cm in height, mounted on the flume bottom. In the present study, the dyeline is also simulated numerically by using the IPTM algorithm. The calculation with the uniformly coarse grid (Figure 6(a)) requires about 22 iterations to get the converged solution for one time step. This will take 3 s CPU for each time step on a HP 735-100 workstation. The time required for the uniformly fine grid calculation (Figure 6(b)) is 293 s CPU with 94 iterations for each time step whereas the locally refined solution (Figure 6(c)) requires 21 s CPU, a 90 per cent reduction in CPU time to the former. Since both solutions has almost the same

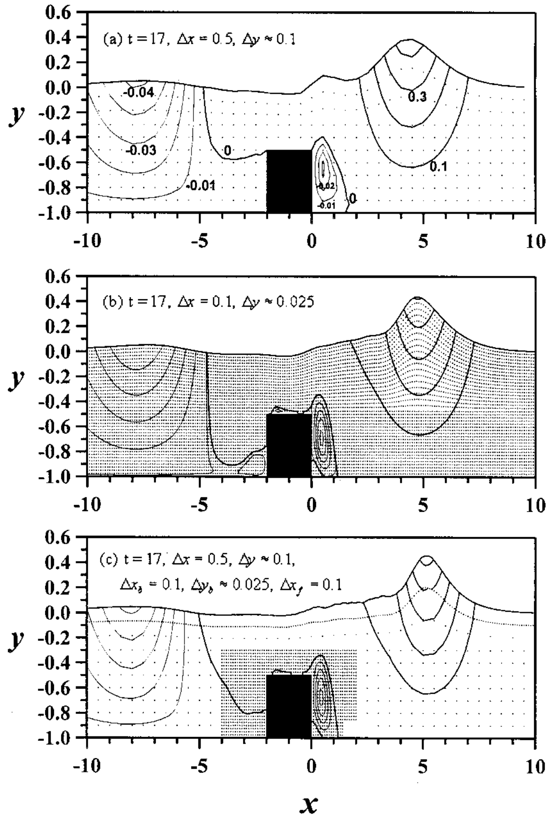

Figure 5. Partial result of grid nodes and streamlines at time $t = 17$ by (a) coarse grid; (b) fine grid; (c) locally refined grid, in which (Δx, Δy) is the base-grid size, and Δx_f and (Δx_b, Δy_b) are refined grid sizes on the free surface and near the body, respectively.

accuracy in good agreement with the experimental observation, the application of the locally refined-grid calculation is, therefore, the most preferable.

A semicircular cylinder is the second example in the analysis. Now consider an incident solitary wave of the same amplitude $A_0 = 0.4$ starting in motion at $x_0 = -10$, a distance of 10 times water depth from the center of cylinder. The partial view of the hybrid grid has already been shown in Figure 4. The base grid has 81×11 nodes with two grid refinements, 81×71 around the body and 401×2 along the free surface. The refined grid around the cylinder is a C-type mesh system by the EG method. The grid in the bluff body region has been refined locally by two varieties, namely, 41×36 nodes and 81×71 nodes, to compare each other. Both results show no large difference in the flow patterns. The solution of 81×71 nodes (with $\Delta\tau = 0.1$) is presented only for the sake of demonstration on the dedicatory flow topology. The evolution of streamlines (on the left column) and equi-vorticity contours (on the right) near the cylinder is shown in Figure 7. The simulations are eventually terminated at $t = 15$. The streamline jitter at the interface between Regions II and III at $t = 15$ is related to the discontinuous resolution among the linking grids but not to the scheme error.

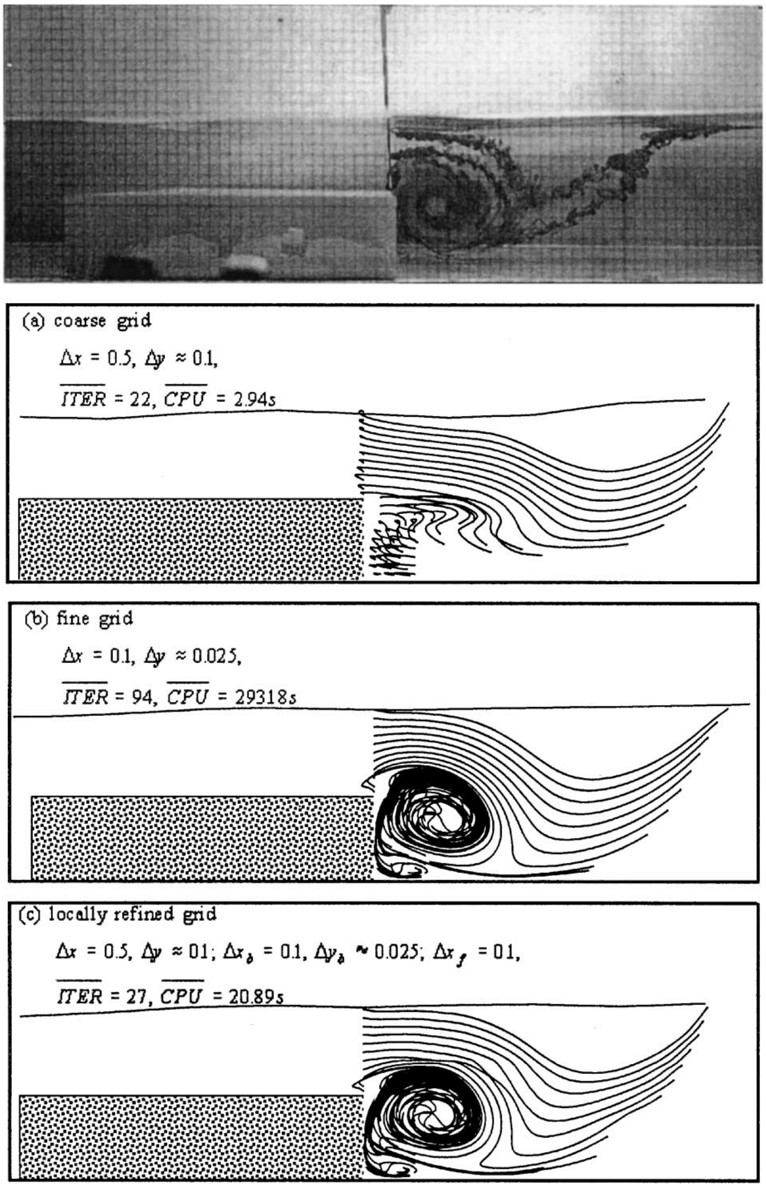

Figure 6. Comparison of streaklines with flow visualization (the upper most figure): (a) coarse grid; (b) fine grid; (c) locally refined grid (where ITER and CPU are iteration number and CPU time respectively, required typically in one time step).

As the solitary wave encounters the cylinder, two wave trains, one for transmission and the other for reflection, are generated. It is noted that the reflection from a semicircular cylinder has much smaller amplitude than that from a rectangle. Complex flow structure is built up during the wave scattering process and is closely related to the wave induced flow separating

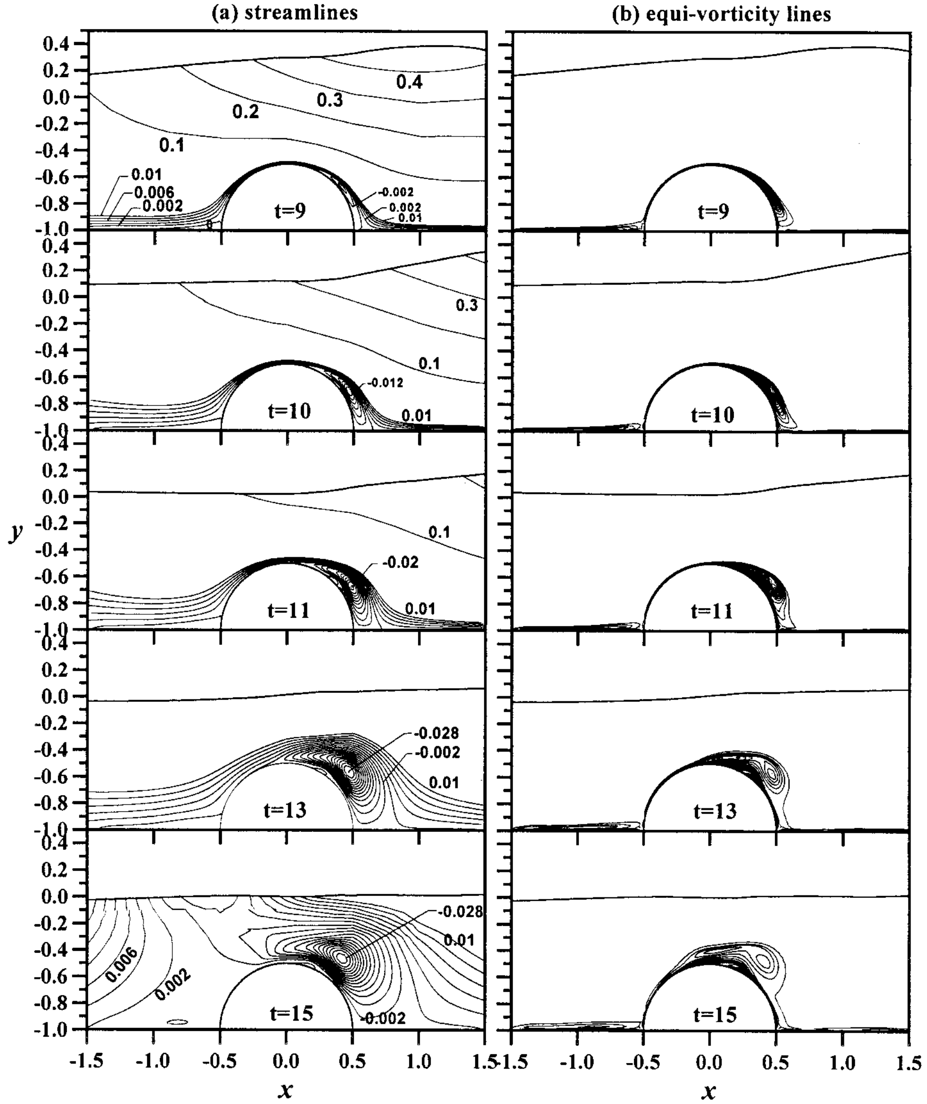

Figure 7. Sequential results of streamlines (left) and equivorticity lines (right) around a semicircular cylinder at times $t = 9$, 10, 11,13 and 15.

from the surface of the bluff body. The vortex structure on the semicircular cylinder is clearly seen in Figure 7. When the wave transmits across over the cylinder, the separation vortex bubble is always kept attached on the rear surface of the cylinder in the analysis. It grows up as the time elapses to increase its strength during the wave-structure interaction. At $t = 13 \sim 15$, the primary vortex is swelling as the transmitted wave moves downstream for a distance apart from the cylinder. At that instance $t = 15$, the backward flow resulting from a small, reflected wave then carries the swelling vortex a little upstream. This vortex motion is different from that caused by the rectangular block, as observed previously in Figure 5. Between both, the most distinct phenomenon is that the separation points slip on the surface of semicircle, but this never happens to the rectangle due to the separation points being almost fixed at the rear convex corner during the vortex growing process.

5. CONCLUSIONS

By using the locally refined grids in our analysis, a hybrid numerical model for the streamfunction–vorticity field was developed with the inviscid–viscous flow schemes. An incident solitary wave passing over two submerged bluff bodies were investigated separately in this paper. The induced vortex motion and the free-surface profile were also illustrated to see the effect of body shape on the phenomena. An evolving curvilinear grid to conform the transient free surface and other boundaries was employed. The results showed that the hybrid model substantially increases the computer efficiency and the solution accuracy. The impressed features during the solitary wave flow interaction with the obstacle were observed using the IPTM technique. These features included the vortex motion and some related flow patterns were discussed briefly.

ACKNOWLEDGEMENTS

This research was partially supported by the National Science Council of ROC under Contract No. NSC88-2611-E006-023.

REFERENCES

1. Antunes-Do-Carmo JS, Seabra-Santos FJ, Barthe’lemy E. Surface waves propagation in shallow water: a finite element model. *International Journal for Numerical Methods in Fluids* 1993; **16**:447–459.
2. Titov VV, Synolakis CE. Modeling of breaking and nonbreaking long-wave evolution and runup using VTCS2. *Journal of Waterway*, *Port*, *Coastal and Ocean Engineering* 1995; **121**(6):308–316.
3. Walkley M, Berzins M. A finite element method for the one-dimensional extended Boussinesq equations. *International Journal for Numerical Methods in Fluids* 1999; **29**:143–157.
4. Gobbi MF, Kirby JT. Wave evolution over submerged sills: tests of high-order Boussinesq model. *Coastal Engineering* 1999; **37**:57–96.
5. Ramaswamy B. Numerical simulation of unsteady viscous flow. *Journal of Computational Physics* 1990; **90**:396–430.
6. Tang CJ, Patel VC, Landweber L. Viscous effects on propagation and reflection of solitary waves in shallow channels. *Journal of Computational Physics* 1990; **88**:86–133.
7. Cooker MJ, Peregrine DH, Vidal C, Dolled JW. The interaction between a solitary wave and a submerged semicircular cylinder. *Journal of Fluid Mechanics* 1990; **215**:1–22.
8. Grilli ST, Subramanya R, Svendsen IA, Veeramony J. Shoaling of solitary waves on plane beaches. *Journal of Waterway*, *Port*, *Coastal and Ocean Engineering* 1994; **120**(6):609–628.
9. Tang CI, Chang JH. Flow separation during a solitary wave passing over a submerged obstacle. *ASCE*, *Journal of Hydraulic Engineering* 1998; **124**(7):732–749.
10. Yih CS. *Fluid Mechanics* (1988 edn). West River Press: Michigan, IL, 1977.
11. Young DP, Melvin RG, Bieterman MB. A locally refined rectangular grid finite element method: application to computational fluid dynamics and computational physics. *Journal of Computational Physics* 1991; **92**:1–66.
12. Trompert R. Local-uniform-grid refinement and transport in heterogeneous porous media. *Advances in Resources* 1993; **16**:293–304.
13. De Lange HC, De Goey LPH. Numerical flow modeling in a locally refined grid. *International Journal for Numerical Methods in Engineering* 1994; **37**:497–515.
14. Dahie HK, Espedal MS, Saevareid O. Characteristic, local grid refinement techniques for reservoir flow problems. *International Journal for Numerical Methods in Engineering* 1992; **34**:1051–1069.

15. Tsiveriotis K, Brown RA. Solution of free-boundary problems using finite-element/Newton methods and locally refined grids: application to analysis of solidification microstructure. *International Journal for Numerical Methods in Fluids* 1993; **16**:827–843.
16. Ryskin G, Leal LG. Numerical solution of free-boundary problems in fluid mechanics. Part 1. The finite-difference technique. *Journal of Fluid Mechanics* 1984; **148**:1–17.
17. Thompson MC, Ferziger JH. An adaptive multigrid technique for the incompressible Navier–Stokes equations. *Journal of Computational Physics* 1989; **82**:94–121.
18. Cleo P, Pereira JCF, Carvalho MG. Calculation of laminar recirculating flows using a local non-staggered grid refinement system. *International Journal for Numerical Methods in Fluids* 1991; **12**:535–557.
19. Tang CJ, Chang JH. Local grid refinement for nonlinear waves. *Journal of the Chinese Institute of Engineers* 1997; **20**(3):285–293.
20. Haussling HJ, Coleman RM. Nonlinear water waves generated by an accelerated circular cylinder. *Journal of Fluid Mechanics* 1979; **92**(4):767–781.
21. Yeung RW, Vaidhyanathan M. Non-linear interaction of water waves with submerged obstacles. *International Journal for Numerical Methods in Fluids* 1992; **14**:1111–1130.
22. Grimshaw R. The solitary wave in water of variable depth, part 1. *Journal of Fluid Mechanics* 1971; **46**(3):611–622.
23. Chen CJ, Chen HC. Finite analytic numerical method for unsteady two-dimensional Navier–Stokes equations. *Journal of Computational Physics* 1984; **53**(2):209–226.
24. Patankar SV. *Numerical Heat Transfer and Fluid Flow*. Hemisphere: New York, 1980.
25. Bernatz RA, Chen CJ, Cekirge HM. Finite analytic solution of a two dimensional sea breeze on a regular grid. *Journal of Mathematical and Computational Modeling* 1994; **19**(1):71–87.
26. Tsai WF, Chen CJ. Unsteady finite-analytic method for solute transport in ground-water flow. *Journal of Engineering and Mechanics* 1995; **121**(2):230–243.
27. Bouard R, Coutanceau M. The early stage of development of the wake behind an impulsively started cylinder for $40 < Re < 10^4$. *Journal of Fluid Mechanics* 1980; **101**(3):583–607.
28. Chang CC, Chern RL. A numerical study of flow around an impulsively started circular cylinder by a deterministic vortex method. *Journal of Fluid Mechanics* 1991; **233**:243–263.
29. Shirayama S. Visualization of 3D unsteady flow using a particle tracing method. *Experimental and Numerical Flow Visualization* 1991; **FED-28**:201–208.